NANO LETTERS

pubs.acs.org/NanoLett Letter

Topological Band Engineering in q-BICs and EPs Derived from Visible Range Plasmons

Wei Li, Cai Luo, Shibing Tian, RuiXuan Zheng, Guangzhou Geng, Haifang Yang, Baoli Liu, Qinghua Song,* Yang Guo,* and Changzhi Gu*

Cite This: *Nano Lett.* 2025, 25, 6117−6124 Read Online

ACCESS | Metrics & More | Article Recommendations | Supporting Information

Downloaded via INST OF PHYSICS on April 17, 2025 at 01:18:44 (UTC).
See https://pubs.acs.org/sharingguidelines for options on how to legitimately share published articles.

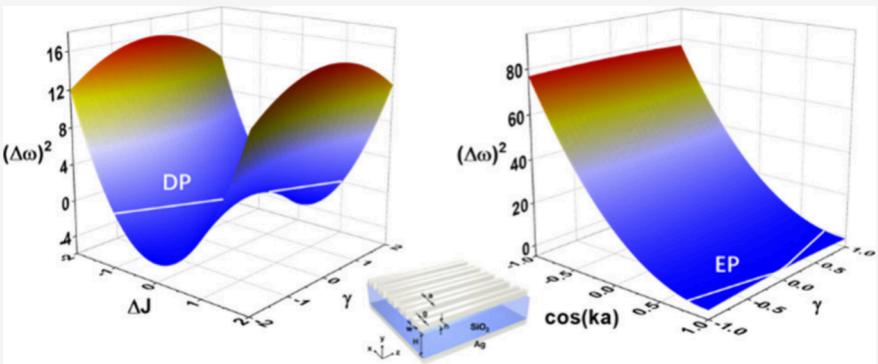

ABSTRACT: Topological photonics, owing to its band topology, has substantial potential in applications such as quantum computation and photonic chips. However, attaining flexible control over band topology for effective light−matter interactions at the subwavelength scale remains elusive. In this study, we present a metal−insulator−metal (MIM) dimerized grating structure based on the one-dimensional (1D) Su−Schrieffer−Heeger model (SSH). This structure is designed for tuning optical band topology with a relatively high quality factor and small mode volume. Specifically, by variation of the grating thickness, topological band inversion with plasmonic quasi-bound states in the continuum (q-BICs) can be achieved. Moreover, through the modulation of gain−loss and coupling strength, the corresponding exceptional points (EPs) can emerge near the Brillouin zone center (Γ point). Consequently, this MIM dimerized grating structure offers a novel approach for the design of advanced topological devices.

KEYWORDS: *q-BIC, EPs, SSH model, band topology*

In recent decades, topological photonics has attracted substantial attention in fields such as optical quantum computation[1,2] and on-chip integration,[3−5] because of its unique features like backscattering-immune propagation[6−8] and topological protected chirality.[9−11] These distinctive topological properties stem from the principles of topological phases and phase transitions in condensed matter physics,[12,13] which underpin the construction of topological edge states and phase modulation. In photonic systems, topological concepts from electronic systems in condensed matter physics can be introduced into photonic crystals and metasurfaces. This is achieved through the direct analogy between the Dirac equation and Maxwell's equation, resulting in nonzero topological invariants in the photonic band structures, such as the Chern number and Z_2 charge.[14−16] A crucial aspect is the connection between topological and non-Hermitian concepts. Photonic systems are usually open and non-Hermitian, in contrast to their conventional Hermitian counterparts. Due to the inclusion of an additional gain−loss factor,[17−19] it can exhibit more diverse optical field manipulation effects. In particular, a significant singularity known as the exceptional point (EP) can emerge in the near-degenerate regime during the parity-time (PT) phase transition in non-Hermitian systems. EPs are branch point singularities arising from the coalescence of eigenvalues and their corresponding eigenvectors. They possess a specific topological phase in parameter space and high sensitivity to perturbations, thus holding promising potential for applications in sensing,[20,21] holograms,[22−24] and chiral laser emission.[25−27]

Generally, topological photonic crystals and metasurfaces can be classified based on different material platforms, primarily focusing on dielectric and metallic nanostructures.[28−31] To date, most of the previous research has been

Received: January 7, 2025
Revised: March 24, 2025
Accepted: March 26, 2025
Published: March 28, 2025

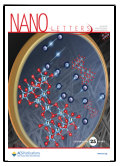

ACS Publications © 2025 American Chemical Society

https://doi.org/10.1021/acs.nanolett.5c00144
Nano Lett. 2025, 25, 6117−6124

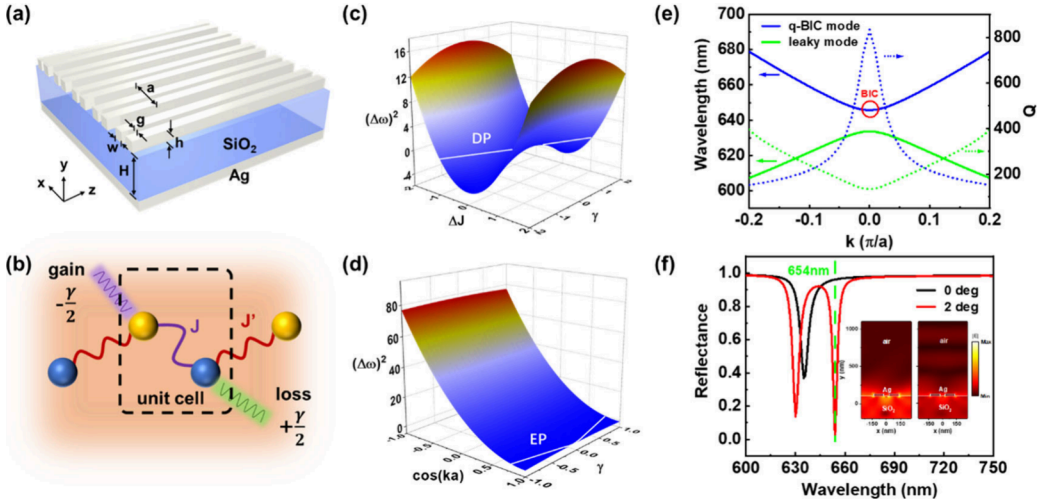

Figure 1. (a) The schematic of the MIM-based nanostructure. (b) The schematic of the 1D SSH model. (c) The square of the bandgap as a function of wavenumber (k) and γ. (d) The square of the bandgap as a function of ΔJ and γ. (e) The band structure (real lines) and the Q factor distribution (dotted lines) of the sample. (f) Simulated reflectance spectra of the sample with different incidence angles (0° and 2°) for TM excitation. Insets: the electric field for 2° at 645 nm (left) and 656 nm (right), respectively.

centered on all-dielectric topological nanostructures, due to their advantages of minimal additional losses and structural integration.[32−34] Nevertheless, considering the widespread application of efficient light−matter interaction, in which topological structures interact with excitonic materials, plasmonic nanostructures with small mode volumes excel in localizing optical fields on subwavelength scales. This property grants them considerable potential for applications in strong coupling at the few-exciton level,[35,36] single-photon emission,[37,38] and entangled state modulation.[39,40] However, there is a significant difference between all dielectric and plasmonic topological nanostructures. In the visible range, plasmonic nanostructures are characterized by low quality (Q) factors of the plasmonic energy bands and relatively small sizes. These characteristics pose obstacles to the modulation of topological phases through structural parameter adjustments in plasmonic nanostructures, thereby further limiting the application of tunable topological devices.

Fortunately, the emergence of bound states in the continuum (BICs) provides a compelling solution to these challenges. As an exotic singularity, BICs are perfectly isolated eigenstates with an infinite Q factor, coexisting with a continuous spectrum of extended states in theory.[41] Experimentally, BICs can be observed through Fano-like resonance in angle-resolved reflectance/transmission spectra.[42−45] In contrast, the Q factor of BICs in open non-Hermitian systems is inevitably finite. For instance, plasmonic BICs possess small mode volumes but relatively low Q factors compared to their dielectric counterparts due to intrinsic losses, thus commonly referred to as plasmonic quasi-BICs.[46] Moreover, BICs exhibit polarization vortex properties in the far-field momentum space,[47−51] which can be utilized to define band topology. Notably, the Su−Schrieffer−Heeger (SSH) model,[52] regarded as a dimerized atomic chain, has been extensively utilized to characterize the band topology of the system.[53−55] Conveniently, band topology with the SSH model can be implemented in a one-dimensional (1D) system by simply tuning the coupling strength, thereby reducing design and processing difficulties.[56] In this paper, we design and fabricate a metal−insulator−metal (MIM) dimerized grating structure to introduce the 1D SSH model, wherein plasmonic quasi-bound states in the continuum (q-BICs) can be observed at the center of the Brillouin zone (Γ point) within the visible spectrum. By varying the grating thickness, the coupling strength can be adjusted, gradually closing the bandgap to form a 1D Dirac point. Subsequently, the bandgap can be reopened, resulting in a topological band inversion. Furthermore, the emergence of EPs can be induced by the collapse of q-BICs, controlled by manipulation of the gain−loss factor and coupling strength. Our results offer a novel approach for controlling singularities and the associated topological phase in plasmonic non-Hermitian optical systems, with potential applications in topological edge state construction,[57−60] topological polaritons,[61−64] and robust wavefront manipulation.[65−67]

To achieve flexible band engineering of plasmonic q-BICs and the emergence of EPs in non-Hermitian optical systems, an MIM-type metasurface featuring a 1D dimerized silver grating on the top was designed and fabricated. As illustrated in Figure 1(a), a 100 nm silver layer at the bottom acts as a mirror, and an amorphous quartz layer with a thickness (H) ranging from 300 to 400 nm was deposited on the silver mirror. Additionally, the periodic dimerized silver gratings with varying thicknesses (h) were fabricated by microfabrication techniques (for details see the Supporting Information). In this plasmonic non-Hermitian system constructed with an MIM configuration, the variation in material thickness plays a key role in band engineering. Specifically, the thickness of the silver grating and the SiO_2 layer are critical for the evolution of transverse magnetic (TM) and transverse electric (TE) bands. The 1D SSH model offers a straightforward, equivalent platform for structural design. As shown in Figure 1(b), this tight-binding model of a 1D SSH model considers only nearest-neighbor interactions with extra gain and loss ($\pm\gamma/2$), where the relative strength of the intracell (J) and intercell (J') couplings determines the topologically trivial and nontrivial phases. In the systems with inversion symmetry, the topological phase (Zak phase) can be quantized to 0 (trivial) or π (nontrivial) for different bands, respectively.[68] In general, the Hamiltonian of the 1D SSH model can be formulated as

https://doi.org/10.1021/acs.nanolett.5c00144
Nano Lett. 2025, 25, 6117−6124

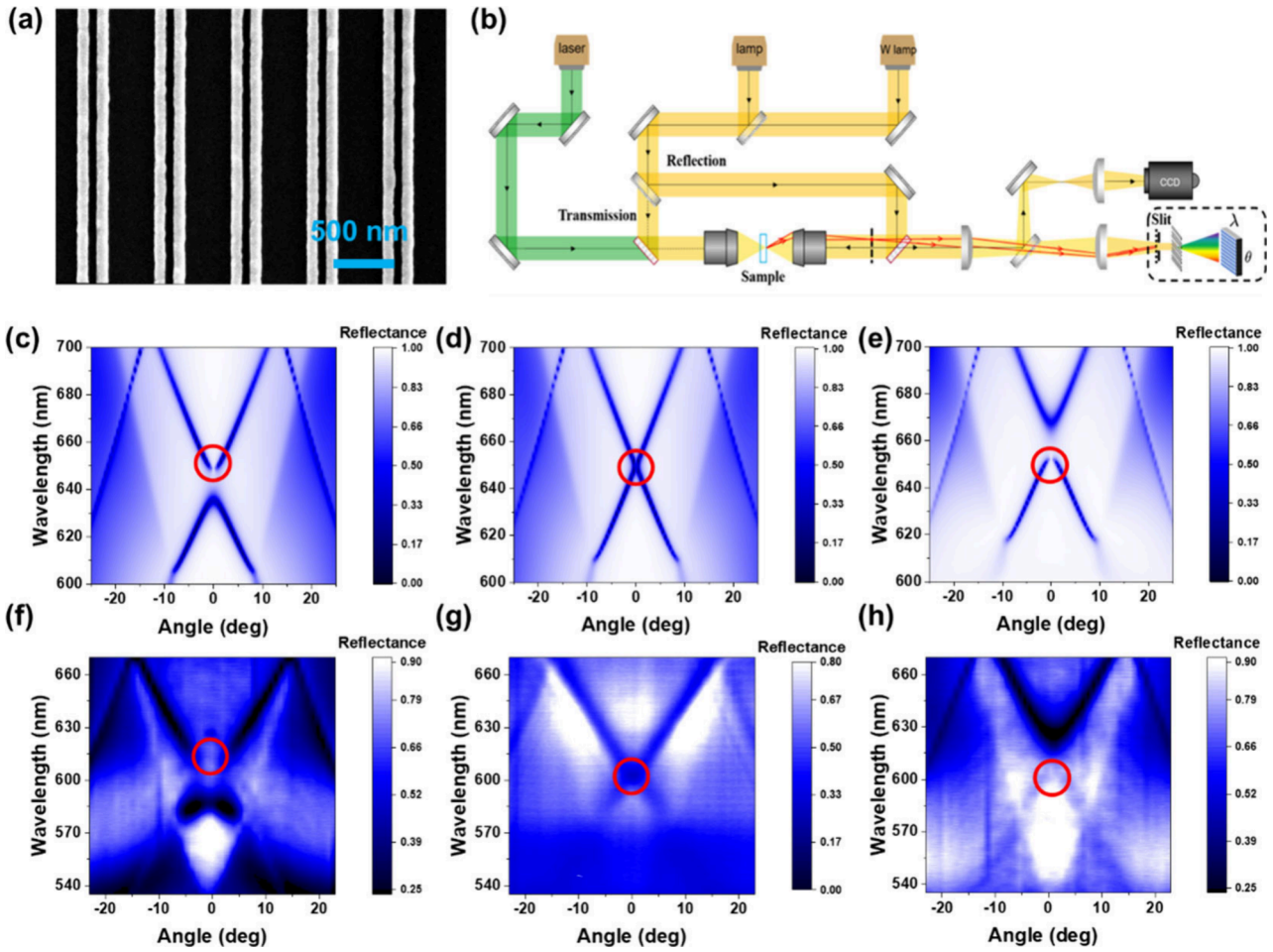

Figure 2. (a) The SEM image of the dimerized silver grating. (b) The schematic of the angle resolved spectra measurement system in the momentum space. (c, d) The simulated angle-resolved reflectance spectra for the samples with different height of the grating ((c) 30 nm, (d) 50 nm, (e) 70 nm). (f–h) The experimental angle-resolved reflectance spectra for samples with different height of the grating ((f) 30 nm, (g) 50 nm, (h) 70 nm).

$$\hat{H}(k) = \begin{bmatrix} \omega_0 - i\frac{\gamma}{2} & J - J'e^{-ika} \\ J - J'e^{ika} & \omega_0 + i\frac{\gamma}{2} \end{bmatrix} \quad (1)$$

where ω_0 represents the resonant frequency, k is the wavenumber, and a denotes the lattice constant. By solving the eigen-equation $\hat{H}(k)\psi(k) = \omega\psi(k)$, the eigen-frequencies can be written as

$$\omega_{\pm} = \omega_0 + \frac{i}{2}\gamma \pm \sqrt{J^2 + J'^2 - 2JJ'\cos(ka) - \left(\frac{\gamma}{2}\right)^2} \quad (2)$$

Evidently, the bandgap ($\Delta\omega = \omega_+ - \omega_-$) can be adjusted by the coupling constants and gain–loss factor, as described by eq 2. Accordingly, Figure 1(c) illustrates the evolution of the $(\Delta\omega)^2$ at the Γ point as a function of ΔJ ($J - J'$) and γ, where the Dirac point (indicated by the white line) represents the degenerate regime (phase transition point). Furthermore, EPs can be induced in the near-degenerate regime by varying the γ. As shown in Figure 1(d), the evolution of $(\Delta\omega)^2$ is presented as a function of $\cos(ka)$ and γ, with the coupling constants fixed at 1 and 1.1, respectively. Clearly, the EPs emerge at $\Delta\omega = 0$, as depicted by the white line. Therefore, it is important to establish the relationship between structural parameters of metasurface, couplings (ΔJ), and loss factors (γ). The emergence of EPs can be effectively controlled through the simultaneous consideration of ΔJ and γ, while the topological inversion based on the BIC may be achieved by considering ΔJ in isolation.

The quasi-normal mode method (QNMs) can be utilized to identify the characteristics of the q-BICs in our system and investigate the band evolution accurately.[69] Initially, the parameters of the corresponding structure are a SiO_2 thickness of $H \sim 350$ nm and silver grating thickness of $h \sim 30$ nm. Figure 1(e) exhibits the eigenmodes calculated numerically. Since this work mainly focuses on plasmonic modes, the band structure is derived from TM excitation, where the electric vector is parallel to the periodic direction. The real lines in Figure 1(e) depict two bands that satisfy the SSH model discussed above. The symmetry-protected BIC is located at the Γ point on the blue line, identified by the red circle (~650 nm), while the corresponding Γ point on the green line represents the leaky mode. The dotted lines in Figure 1(e) display the Q factor of the two bands. It is evident that the Q factor at the BIC is significantly higher than that of the leaky mode, although it is not infinite due to the intrinsic loss of the metal. Therefore, the plasmonic BICs can be considered as q-BICs in nature. To further identify the symmetry-protected q-BICs further, the angle-resolved reflectance spectrum was

https://doi.org/10.1021/acs.nanolett.5c00144
Nano Lett. 2025, 25, 6117–6124

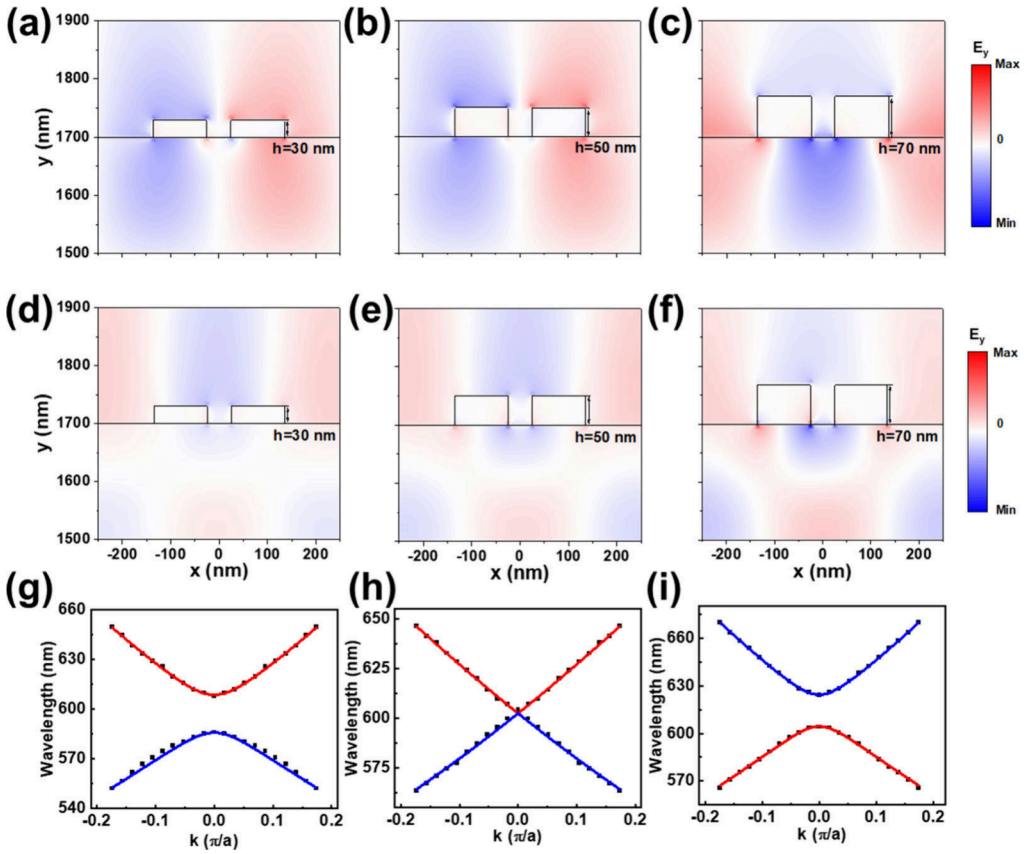

Figure 3. (a–c) The eigen-electric field (E_y) of the higher energy band at the Γ point with different heights of the grating ((a) 30 nm, (b) 50 nm, (c) 70 nm). (d–f) The eigen-electric field (E_y) of the higher energy band at the X point with different heights of the grating ((d) 30 nm, (e) 50 nm, (f) 70 nm). (g–i) The experimental energy band (dots) and fitted by the 1D SSH model (red line and blue line) with different heights of the grating ((g) 30 nm, (h) 50 nm, (i) 70 nm).

simulated by the finite element method (see the Supporting Information). As illustrated in Figure 1(f), two reflectance spectra were calculated for TM excitation at incident angles of 0° and 2°. A distinct Fano-like resonance is observed at 654 nm for the 2° incident angle due to additional radiation loss caused by mode symmetry breaking. The vertical cross sections of the simulated electric field in the near-BIC regime at 654 nm and 2° are depicted in the inset (left) of Figure 1(f), showing that the electric field is predominantly localized at the corner of the silver grating with minimal radiation into the air, confirming the plasmonic nature of this BIC. To further determine the mechanism underlying the generation of this q-BIC, the multipole expansion of the metasurface under different incident angles is performed. These results indicate that the plasmonic q-BIC mainly originates from the electric quadrupole mode (for details see the Supporting Information). Meanwhile, the inset (right) of Figure 1(f) presents the vertical cross sections of the simulated electric field at 656 nm and 2°, suggesting that even a slight deviation (2 nm) from the near-BIC regime could result in significant radiation into the air and a dramatic reduction in the electric field enhancement. Additionally, the detailed influences of structural parameters on the q-BICs are provided in the Supporting Information (Figure S2).

It is necessary to manipulate the intracell couplings in our system in order to observe the band evolution by varying the thickness (h) of the silver gratings ranging from 30 to 70 nm while other structural parameters are fixed ($H \sim 350$ nm). The home-built angle-resolved reflectance spectra measurement system for the corresponding samples is depicted in Figure 2(b), with samples, whose SEM image is shown in Figure 2(a), pasted on the sample table (for details, see the Supporting Information). To begin with, the simulated angle-resolved reflectance spectra with the incident angle ranging from −25° to 25° for TM excitation were calculated, as shown in Figure 2(c)–(e). It is clear that there is a "white point" (high-reflectance point) in the band as marked by a red circle. This is an important feature in the generation of BICs. As depicted in Figure 2(c), the symmetry-protected plasmonic BIC is located at the Γ point of the lower-energy band (upper band) with a bandgap of approximately 13 nm. The intracell couplings can be enhanced via increasing the thickness of the gratings, as the electric field is more likely to be localized in the gap of the dimerized unit. As the thickness of the grating increases, the bandgap narrows. As shown in Figure 2(d), the bandgap closes completely at a grating thickness of 50 nm, resulting in a Dirac point at 650 nm. With further increment in the grating thickness, the bandgap reopens. As shown in Figure 2(e), the bandgap measures approximately 20 nm at a grating thickness of 70 nm. In contrast to the former case shown in Figure 2(c), the symmetry-protected plasmonic BIC is located at the Γ point of the higher-energy band (lower band) instead. These results suggest the need for topological band inversion. As shown in Figure 2(f)–(h), the experimental results are satisfied with the simulation results, where the deviation of the experimental BIC is attributed to the errors in sample

https://doi.org/10.1021/acs.nanolett.5c00144
Nano Lett. 2025, 25, 6117–6124

preparation. Besides, the Q factor of the q-BICs is more than 70, which can be derived from the experimental angle resolved reflectance spectra (for details, see the Supporting Information). The discussions presented above are all based on TM excitations in the samples. Furthermore, the TE excitations where the electric vector is perpendicular to the periodic direction are also studied, as shown in Figure S4 (see the Supporting Information).

To verify the topological band inversion straightforwardly, the eigen-electric field at the Γ point and the boundary of the Brillouin zone (X point) were calculated, as shown in Figure 3(a)−(f). The symmetry of the electric field at the high symmetry points in the Brillouin zone (Γ and X points) is a crucial principle for a certain topological phase. Without loss of generality, the y component (perpendicular to the structure surface) of the eigen-electric field at the Γ and X points of the higher-energy band is considered. It is evident that the symmetry of the electric field at the Γ point changes from odd to even during the band inversion. In contrast, the symmetry of the electric field at the X point remains even throughout the phase transition, signifying that the Zak phase of the higher-energy band shifts from π to 0 during the topological band inversion. To determine the coupling constants, the 1D SSH model was used to fit the experimental energy band, as shown in Figure 3(g)−(i). For simplicity, Hamiltonian (1) can be written with γ ignored. By solving the eigen-equation $\hat{H}(k)\psi(k) = \omega\psi(k)$, the eigen-frequency can thus be written as

$$\omega_{\pm} = \omega_0 \pm \sqrt{J^2 + J'^2 - 2JJ'\cos(ka)} \tag{3}$$

This equation can be utilized to fit the energy band and determine the values of J and J'. In Figure 3(g), $|J|$ and $|J'|$ are 68.29 and 77.72, respectively, satisfying $|J| < |J'|$, indicating a topologically nontrivial phase. In Figure 3(h), $|J| = |J'| = 62.65$, corresponding to the phase transition point. In Figure 3(i), the $|J|$ and $|J'|$ are 77.58 and 69.86, respectively, satisfying $|J| > |J'|$, indicating a topologically trivial phase. These results demonstrate that the nanostructure that we proposed complies with the SSH model.

Furthermore, the band engineering discussed above is grounded in the 1D SSH model, which does not involve tuning the diagonal terms of the Hamiltonian. Consequently, the topological transition point in Figure 3(h) is fundamentally a degenerate Dirac point. To construct an EP in our system, diagonal terms are taken into account. In this two-energy system, the different energy loss γ_1 and γ_2 can be introduced in a specific scenario; thus the Hamiltonian of the 1D SSH model can be written as

$$\hat{H}(k) = \begin{bmatrix} \omega_0 - i\frac{\gamma_1}{2} & J - J'e^{-ika} \\ J - J'e^{ika} & \omega_0 - i\frac{\gamma_2}{2} \end{bmatrix} \tag{4}$$

Without loss of generality, the constant matrix $\begin{bmatrix} -i\frac{\gamma_1+\gamma_2}{4} & 0 \\ 0 & -i\frac{\gamma_1+\gamma_2}{4} \end{bmatrix}$ can be extracted from eq 4 as the background. Subsequently, the remaining Hamiltonian can be formulated in the form of eq 1, where $\gamma = \frac{\gamma_1-\gamma_2}{2}$, representing the non-Hermitian PT symmetry system with generalized gain $(+\frac{\gamma}{2})$ and loss $(-\frac{\gamma}{2})$ factor, providing a new dimension for band engineering.

The emergence of the EPs depends on the coupling constants (J, J') and the system gain−loss factor $(\pm\frac{\gamma}{2})$, which can be manipulated by the structural parameters. Specifically, the EPs occur at the position $\cos(ka) = \frac{J^2+J'^2-(\gamma/2)^2}{2JJ'}$ if the condition $|J - J'| < \frac{\gamma}{2}$ is satisfied. To meet the EPs' condition, some structural parameters of the dimerized MIM grating are adjusted as follows: period (a) is 523 nm, SiO_2 thickness (H) is 300 nm, the height of the grating (h) is 50 nm, and the gap in the unit (g) is 50 nm. The band structure of the sample was simulated by QNMs (black dots) and fitted with the 1D SSH model, including gain−loss (red and blue lines) to determine the coupling constants and the gain−loss factor, as shown in Figure 4. In Figure 4(a), the real part of the band was

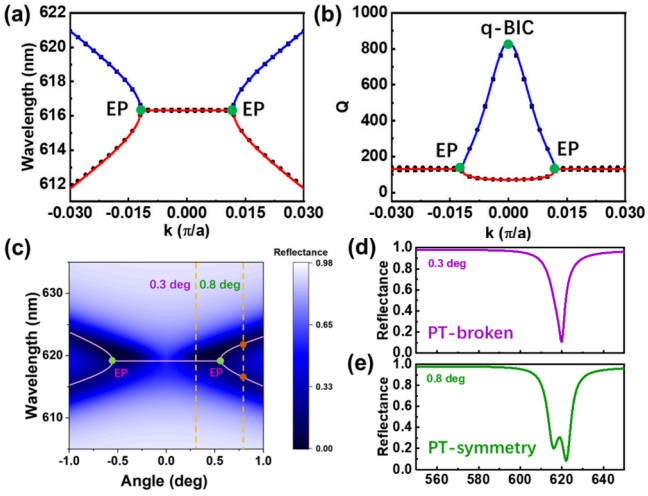

Figure 4. (a) The real part of the band structure in the near-degenerate region. (b) The distribution of the Q factor (dots: calculated by QNMs; red lines (higher frequency) and blue lines (lower frequency): fitted by the 1D SSH model). (c) The simulated angle-resolved reflectance spectra in the near-degenerate region. (d) The reflectance spectra at the incident angle of 0.3 deg. (e) The reflectance spectra at the incident angle of 0.8 deg.

numerically calculated in which a flat degenerate line extends around the center of the Γ point and ends at the point $k = \pm 0.0119\ \pi/a$. According to the fitted lines by the 1D SSH model, the gain−loss factor $\gamma \approx 3.725$ THz and the coupling constants satisfy $|J - J'| \approx 1$, fulfilling the EPs' emergence condition $|J - J'| < \frac{\gamma}{2}$. In Figure 4(b), the distribution of the Q factor in momentum space is carried out. It is evident that the Q factors of the two modes differ significantly at the Γ point. The lower frequency mode (blue line) with a higher Q factor corresponds to the q-BIC mode, while the higher frequency mode (red line) represents the leaky mode. Furthermore, the Q factors of both modes gradually become degenerate since wavenumber $|k|$ exceeds $0.0119\pi/a$, implicating that the points $k = \pm 0.0119\ \pi/a$ are the phase transition points for the Q factor. Certainly, based on the fitted results from the SSH model, the points $k = \pm 0.0119\ \pi/a$ satisfy the EPs' position where $\cos(ka) = \frac{J^2+J'^2-(\gamma/2)^2}{2JJ'} = 0.9993$, thus satisfying the degeneracy of the real and imaginary parts of the

https://doi.org/10.1021/acs.nanolett.5c00144
Nano Lett. 2025, 25, 6117−6124

modes. To further demonstrate the experimental feasibility of EPs, the simulated angle-resolved reflectance spectra in the near-degenerate regime are performed. As shown in Figure 4(c), it is evident that a pair of phase transition points emerged at the incident angle of 0.6 deg, which is consistent with the results of QNMs. Additionally, Figures 4(d) and (e) present the reflectance spectra at incident angles of 0.3° and 0.8°, corresponding to the PT-broken phase and the PT-symmetric phase, respectively. Therefore, it is a convenient approach to manipulate the q-BICs and EPs in a plasmonic system by mainly adjusting the thickness of the structure layer, significantly simplifying the design of topological non-Hermitian optical devices.

In conclusion, an MIM-type dimerized grating was successfully designed and fabricated to realize the band engineering of the plasmonic q-BICs and EPs in the visible range. Benefiting from the 1D SSH model, the bandgap of the TM band can be flexibly manipulated, and the topological phase transition of the q-BICs can be achieved by adjusting the coupling constants. Additionally, the introduction of the gain−loss factor into the SSH model as a new manipulation dimension allows for the emergence of EPs near the q-BICs by simultaneous control of the coupling constants and gain−loss factor. Our precise construction of the nanostructure based on the SSH model offers a novel approach to band topology engineering. This not only paves the way for the creation of topological edge states and robust topological phase modulation but also holds great promise for the development of novel photonic devices with enhanced functionality. For instance, topological photonic devices based on q-BICs and EPs can enable strong coupling at the few-exciton level, crucial for quantum state control. Also, they can contribute to more reliable single-photon sources in single-photon emission and are applicable in entangled state modulation, which is fundamental for quantum communication and computing.

■ ASSOCIATED CONTENT

Supporting Information

The Supporting Information is available free of charge at https://pubs.acs.org/doi/10.1021/acs.nanolett.5c00144.

Additional information about the device fabrication method, the simulation method for calculating the plasmonic BICs and EPs, the details of the optical measurement, the multipole expansion under different incident angles, the simulations of the structural parameter influence, the Q factor of plasmonic q-BIC, the simulated angle-resolved reflectance spectrum for TE excitation, and the simulated eigen-electric field of the lower energy band (PDF)

■ AUTHOR INFORMATION

Corresponding Authors

Changzhi Gu − *Beijing National Laboratory for Condensed Matter Physics, Institute of Physics, Chinese Academy of Sciences, Beijing 100190, China; School of Physical Sciences, CAS Key Laboratory of Vacuum Physics, University of Chinese Academy of Sciences, Beijing 100190, China;* orcid.org/0000-0002-2689-2807; Email: czgu@iphy.ac.cn

Yang Guo − *Beijing National Laboratory for Condensed Matter Physics, Institute of Physics, Chinese Academy of Sciences, Beijing 100190, China; School of Physical Sciences, CAS Key Laboratory of Vacuum Physics, University of Chinese Academy of Sciences, Beijing 100190, China;* orcid.org/0000-0001-8975-9387; Email: yangguo@iphy.ac.cn

Qinghua Song − *Tsinghua Shenzhen International Graduate School, Tsinghua University, Shenzhen 518055, China; Suzhou Laboratory, Suzhou 215000, China;* orcid.org/0000-0002-4622-0418; Email: song.qinghua@sz.tsinghua.edu.cn

Authors

Wei Li − *Beijing National Laboratory for Condensed Matter Physics, Institute of Physics, Chinese Academy of Sciences, Beijing 100190, China; Tsinghua Shenzhen International Graduate School, Tsinghua University, Shenzhen 518055, China;* orcid.org/0009-0003-8370-7705

Cai Luo − *Beijing National Laboratory for Condensed Matter Physics, Institute of Physics, Chinese Academy of Sciences, Beijing 100190, China; Key Laboratory for Microstructural Material Physics of Hebei Province, School of Science, Yanshan University, Qinhuangdao 066004, China*

Shibing Tian − *Beijing National Laboratory for Condensed Matter Physics, Institute of Physics, Chinese Academy of Sciences, Beijing 100190, China*

RuiXuan Zheng − *New Cornerstone Science Laboratory, Department of Physics, University of Hong Kong, Hong Kong 999077, China*

Guangzhou Geng − *Beijing National Laboratory for Condensed Matter Physics, Institute of Physics, Chinese Academy of Sciences, Beijing 100190, China*

Haifang Yang − *Beijing National Laboratory for Condensed Matter Physics, Institute of Physics, Chinese Academy of Sciences, Beijing 100190, China*

Baoli Liu − *Beijing National Laboratory for Condensed Matter Physics, Institute of Physics, Chinese Academy of Sciences, Beijing 100190, China; School of Physical Sciences, CAS Key Laboratory of Vacuum Physics, University of Chinese Academy of Sciences, Beijing 100190, China; CAS Center for Excellence in Topological Quantum Computation, CAS Key Laboratory of Vacuum Physics University of Chinese Academy of Sciences, Beijing 100190, China; Songshan Lake Materials Laboratory, Dongguan, Guangdong 523808, China*

Complete contact information is available at: https://pubs.acs.org/10.1021/acs.nanolett.5c00144

Author Contributions

W.L., C.L., and S.B.T. contributed equally to this work. W.L., Y.G., and C.L. conceived the ideas and designed the experiments. W.L. and S.B.T. prepared the samples. Y.G. and C.L. carried out the optical spectroscopy measurements. Y.G., W.L., and C.L. analyzed the data. Y.G., Q.H.S., and W.L. wrote the manuscript with input from all authors.

Notes

The authors declare no competing financial interest.

■ ACKNOWLEDGMENTS

This work was supported by the National Key Research and Development Program of China under Grant Nos. 2024YFA-1207700, 2022YFA1204100, and 2021YFA1400700; National Natural Science Foundation of China under Grants Nos. 92265110, 62174179, 62204259, 12474388, and 12204264;

Strategic Priority Research Program of the Chinese Academy of Sciences under Grant No. XDB33020200; and Guangdong Basic and Applied Basic Research Foundation under Grant No. 2025A1515011483. This work was also supported by the Micro/nano Fabrication Laboratory of Synergetic Extreme Condition User Facility (SECUF).

REFERENCES

(1) Joo, J.; Alba, E.; García-Ripoll, J. J.; Spiller, T. P. Generating and verifying graph states for fault-tolerant topological measurement-based quantum computing in two-dimensional optical lattices. *Phys. Rev. A* **2013**, *88* (1), 012328−012333.
(2) He, L.; Liu, D.; Zhang, H.; Zhang, F.; Zhang, W.; Feng, X.; Huang, Y.; Cui, K.; Liu, F.; Zhang, W.; Zhang, X. Topologically protected quantum logic gates with valley-Hall photonic crystals. *Adv. Mater.* **2024**, *36* (24), 2311611−2311618.
(3) Xu, B.-C.; Xie, B.-Y.; Xu, L.-H.; Deng, M.; Chen, W.; Wei, H.; Dong, F.; Wang, J.; Qiu, C.-W.; Zhang, S.; Chen, L. Topological Landau-Zener nanophotonic circuits. *Advanced Photonics* **2023**, *5* (03), 036005−036012.
(4) Dai, T.; Ma, A.; Mao, J.; Ao, Y.; Jia, X.; Zheng, Y.; Zhai, C.; Yang, Y.; Li, Z.; Tang, B.; Luo, J.; Zhang, B.; Hu, X.; Gong, Q.; Wang, J. A programmable topological photonic chip. *Nat. Mater.* **2024**, *23* (7), 928−936.
(5) Liu, X.; Kan, Y.; Kumar, S.; Komisar, D.; Zhao, C.; Bozhevolnyi, S. I. On-chip generation of single-photon circularly polarized single-mode vortex beams. *Science Advances* **2023**, *9* (32), No. eadh0725.
(6) Guo, Y.; Dekorsy, T.; Hettich, M. Topological guiding of elastic waves in phononic metamaterials based on 2D pentamode structures. *Sci. Rep.* **2017**, *7* (1), 18043−18049.
(7) Swinteck, N.; Matsuo, S.; Runge, K.; Vasseur, J. O.; Lucas, P.; Deymier, P. A. Bulk elastic waves with unidirectional backscattering-immune topological states in a time-dependent superlattice. *J. Appl. Phys.* **2015**, *118* (6), 063103−063110.
(8) Fan, X.; Zhou, B. Anti-scattering propagation in multiple-bend valley phononic crystals. *New J. Phys.* **2024**, *26* (5), 053043−053049.
(9) Cao, Y.; Sheng, L.; Zhou, Q.; Wang, R.; Chen, Z.; Ling, X. Chirality-enabled topological phase transitions in parity-time symmetric systems. *New J. Phys.* **2024**, *26* (6), 063040−063050.
(10) Cai, S.; Chen, J.; Liu, X.; Fu, G.; Liu, G.; Chen, J.; Tang, C.; Du, W.; Liu, Z. Perfect intrinsic and nonlinear chirality simultaneously driven by half-integer topological charge. *Phys. Rev. B* **2024**, *109* (16), 165420−165429.
(11) Chen, Y.; Deng, H.; Sha, X.; Chen, W.; Wang, R.; Chen, Y.-H.; Wu, D.; Chu, J.; Kivshar, Y. S.; Xiao, S.; Qiu, C.-W. Observation of intrinsic chiral bound states in the continuum. *Nature* **2023**, *613* (7944), 474−478.
(12) Thouless, D. J.; Kohmoto, M.; Nightingale, M. P.; den Nijs, M. Quantized Hall conductance in a two-dimensional periodic potential. *Phys. Rev. Lett.* **1982**, *49* (6), 405−408.
(13) KOHMOTO, M. Topological department invariant and the quantization of the Hall conductance. *Annals of Physics* **1985**, *160* (2), 343−354.
(14) Wang, Z.; Chong, Y.; Joannopoulos, J. D.; Soljačić, M. Observation of unidirectional backscattering-immune topological electromagnetic states. *Nature* **2009**, *461* (7265), 772−775.
(15) Skirlo, S. A.; Lu, L.; Igarashi, Y.; Yan, Q.; Joannopoulos, J.; Soljačić, M. Experimental observation of large Chern numbers in photonic crystals. *Phys. Rev. Lett.* **2015**, *115* (25), 253901−253906.
(16) Wu, L.-H.; Hu, X. Scheme for achieving a topological photonic crystal by using dielectric material. *Phys. Rev. Lett.* **2015**, *114* (22), 223901−223905.
(17) Chen, M. L. N.; Jiang, L. J.; Zhang, S.; Zhao, R.; Lan, Z.; Sha, W. E. I. Comparative study of Hermitian and non-Hermitian topological dielectric photonic crystals. *Phys. Rev. A* **2021**, *104* (3), 033501−033506.
(18) Takata, K.; Notomi, M. Photonic topological insulating phase induced solely by gain and loss. *Phys. Rev. Lett.* **2018**, *121* (21), 213902−213907.
(19) Wetter, H.; Fleischhauer, M.; Linden, S.; Schmitt, J. Observation of a topological edge state stabilized by dissipation. *Phys. Rev. Lett.* **2023**, *131* (8), 083801−083806.
(20) Chen, W.; Kaya Özdemir, Ş.; Zhao, G.; Wiersig, J.; Yang, L. Exceptional points enhance sensing in an optical microcavity. *Nature* **2017**, *548* (7666), 192−196.
(21) Wiersig, J. Sensors operating at exceptional points: General theory. *Phys. Rev. A* **2016**, *93* (3), 033809−033817.
(22) Song, Q.; Odeh, M.; Zúñiga-Pérez, J.; Kanté, B.; Genevet, P. Plasmonic topological metasurface by encircling an exceptional point. *Science* **2021**, *373* (6559), 1133−1137.
(23) Yang, Z.; Huang, P.-S.; Lin, Y.-T.; Qin, H.; Chen, J.; Han, S.; Huang, W.; Deng, Z.-L.; Li, B.; Zúñiga-Pérez, J.; Genevet, P.; Wu, P. C.; Song, Q. Asymmetric full-color vectorial meta-holograms empowered by pairs of exceptional points. *Nano Lett.* **2024**, *24* (3), 844−851.
(24) Hu, S.; Wang, C.; Du, S.; Han, Z.; Gu, C. Dynamic and polarization-independent wavefront control based on hybrid topological metasurfaces. *Nano Lett.* **2024**, *24* (6), 2041−2047.
(25) Gadasi, S.; Arwas, G.; Gershenzon, I.; Friesem, A.; Davidson, N. Chiral states in coupled-lasers lattice by on-site complex potential. *Phys. Rev. Lett.* **2022**, *128* (16), 163901−163906.
(26) Hayenga, W. E.; Parto, M.; Ren, J.; Wu, F. O.; Hokmabadi, M. P.; Wolff, C.; El-Ganainy, R.; Mortensen, N. A.; Christodoulides, D. N.; Khajavikhan, M. Direct generation of tunable orbital angular momentum beams in microring lasers with broadband exceptional points. *ACS Photonics* **2019**, *6* (8), 1895−1901.
(27) Ji, K.; Zhong, Q.; Ge, L.; Beaudoin, G.; Sagnes, I.; Raineri, F.; El-Ganainy, R.; Yacomotti, A. M. Tracking exceptional points above the lasing threshold. *Nat. Commun.* **2023**, *14* (1), 8304−8312.
(28) Khanikaev, A. B.; Hossein Mousavi, S.; Tse, W.-K.; Kargarian, M.; MacDonald, A. H.; Shvets, G. Photonic topological insulators. *Nat. Mater.* **2013**, *12* (3), 233−239.
(29) Slobozhanyuk, A.; Mousavi, S. H.; Ni, X.; Smirnova, D.; Kivshar, Y. S.; Khanikaev, A. B. Three-dimensional all-dielectric photonic topological insulator. *Nat. Photonics* **2017**, *11* (2), 130−136.
(30) Wu, X.; Meng, Y.; Tian, J.; Huang, Y.; Xiang, H.; Han, D.; Wen, W. Direct observation of valley-polarized topological edge states in designer surface plasmon crystals. *Nat. Commun.* **2017**, *8* (1), 1304−1312.
(31) Gao, F.; Xue, H.; Yang, Z.; Lai, K.; Yu, Y.; Lin, X.; Chong, Y.; Shvets, G.; Zhang, B. Topologically protected refraction of robust kink states in valley photonic crystals. *Nat. Phys.* **2018**, *14* (2), 140−144.
(32) Shalaev, M. I.; Walasik, W.; Tsukernik, A.; Xu, Y.; Litchinitser, N. M. Robust topologically protected transport in photonic crystals at telecommunication wavelengths. *Nat. Nanotechnol.* **2019**, *14* (1), 31−34.
(33) Chen, X.-D.; Zhao, F.-L.; Chen, M.; Dong, J.-W. Valley-contrasting physics in all-dielectric photonic crystals: Orbital angular momentum and topological propagation. *Phys. Rev. B* **2017**, *96* (2), 020202−020206.
(34) Chen, X.-D.; Shi, F.-L.; Liu, H.; Lu, J.-C.; Deng, W.-M.; Dai, J.-Y.; Cheng, Q.; Dong, J.-W. Tunable electromagnetic flow control in valley photonic crystal waveguides. *Physical Review Applied* **2018**, *10* (4), 044002−044009.
(35) Qin, J.; Chen, Y.-H.; Zhang, Z.; Zhang, Y.; Blaikie, R. J.; Ding, B.; Qiu, M. Revealing strong plasmon-exciton coupling between nanogap resonators and two-dimensional semiconductors at ambient conditions. *Phys. Rev. Lett.* **2020**, *124* (6), 063902−063907.
(36) Liu, L.; Tobing, L. Y. M.; Wu, T.; Qiang, B.; Garcia-Vidal, F. J.; Zhang, D. H.; Wang, Q. J.; Luo, Y. Plasmon-induced thermal tuning of few-exciton strong coupling in 2D atomic crystals. *Optica* **2021**, *8* (11), 1416−1423.
(37) Sáez-Blázquez, R.; Cuartero-González, Á.; Feist, J.; García-Vidal, F. J.; Fernández-Domínguez, A. I. Plexcitonic quantum light

https://doi.org/10.1021/acs.nanolett.5c00144
Nano Lett. 2025, 25, 6117−6124

emission from nanoparticle-on-mirror cavities. *Nano Lett.* **2022**, *22* (6), 2365−2373.
(38) Xie, L.; Yang, H.; Yang, Y.; Chen, Z.; Li, H.; Li, Z.; Liu, D. Multiphoton emission of single CdZnSe/ZnS quantum dots coupled with plasmonic Au nanoparticles. *Phys. Chem. Chem. Phys.* **2024**, *26* (6), 5607−5614.
(39) Pompe, R.; Hensen, M.; Otten, M.; Gray, S. K.; Pfeiffer, W. Pure dephasing induced single-photon parametric down-conversion in a strongly coupled plasmon-exciton system. *Phys. Rev. B* **2023**, *108* (11), 115432−115443.
(40) Gubin, M. Y.; Shesterikov, A. V.; Karpov, S. N.; Prokhorov, A. V. Entangled plasmon generation in nonlinear spaser system under the action of external magnetic field. *Phys. Rev. B* **2018**, *97* (8), 085431−085445.
(41) Hsu, C. W.; Zhen, B.; Stone, A. D.; Joannopoulos, J. D.; Soljačić, M. Bound states in the continuum. *Nature Reviews Materials* **2016**, *1* (9), 16048−16060.
(42) Sadrieva, Z. F.; Sinev, I. S.; Koshelev, K. L.; Samusev, A.; Iorsh, I. V.; Takayama, O.; Malureanu, R.; Bogdanov, A. A.; Lavrinenko, A. V. Transition from optical bound states in the continuum to leaky resonances: role of substrate and roughness. *ACS Photonics* **2017**, *4* (4), 723−727.
(43) Azzam, S. I.; Shalaev, V. M.; Boltasseva, A.; Kildishev, A. V. Formation of bound states in the continuum in hybrid plasmonic-photonic systems. *Phys. Rev. Lett.* **2018**, *121* (25), 253901−253906.
(44) Li, S.; Zhou, C.; Liu, T.; Xiao, S. Symmetry-protected bound states in the continuum supported by all-dielectric metasurfaces. *Phys. Rev. A* **2019**, *100* (6), 063803−063808.
(45) Shi, T.; Deng, Z.-L.; Tu, Q.-A.; Cao, Y.; Li, X. Displacement-mediated bound states in the continuum in all-dielectric superlattice metasurfaces. *PhotoniX* **2021**, *2* (1), 7−16.
(46) Liang, Y.; Koshelev, K.; Zhang, F.; Lin, H.; Lin, S.; Wu, J.; Jia, B.; Kivshar, Y. Bound states in the continuum in anisotropic plasmonic metasurfaces. *Nano Lett.* **2020**, *20* (9), 6351−6356.
(47) Zhang, Y.; Chen, A.; Liu, W.; Hsu, C. W.; Wang, B.; Guan, F.; Liu, X.; Shi, L.; Lu, L.; Zi, J. Observation of polarization vortices in momentum space. *Phys. Rev. Lett.* **2018**, *120* (18), 186103−186108.
(48) Hsu, C. W.; Zhen, B.; Lee, J.; Chua, S.-L.; Johnson, S. G.; Joannopoulos, J. D.; Soljačić, M. Observation of trapped light within the radiation continuum. *Nature* **2013**, *499* (7457), 188−191.
(49) Doeleman, H. M.; Monticone, F.; den Hollander, W.; Alù, A.; Koenderink, A. F. Experimental observation of a polarization vortex at an optical bound state in the continuum. *Nat. Photonics* **2018**, *12* (7), 397−401.
(50) Shi, T.; Deng, Z. L.; Geng, G.; Zeng, X.; Zeng, Y.; Hu, G.; Overvig, A.; Li, J.; Qiu, C. W.; Alu, A.; Kivshar, Y. S.; Li, X. Planar chiral metasurfaces with maximal and tunable chiroptical response driven by bound states in the continuum. *Nat. Commun.* **2022**, *13* (1), 4111−4118.
(51) Li, F.-J.; Wang, S.; Zhong, R.; Hu, M.-X.; Jiang, Y.; Zheng, M.; Wang, M.; Li, X.; Peng, R.; Deng, Z.-L. Metasurface polarization optics: From classical to quantum. *Applied Physics Reviews* **2024**, *11* (4), 041332−041363.
(52) Su, W. P.; Schrieffer, J. R.; Heeger, A. J. Solitons in polyacetylene. *Phys. Rev. Lett.* **1979**, *42* (25), 1698−1701.
(53) Heeger, A. J.; Kivelson, S.; Schrieffer, J. R.; Su, W. P. Solitons in conducting polymers. *Rev. Mod. Phys.* **1988**, *60* (3), 781−850.
(54) Liu, C.; Ong, H. C. Realization of topological superlattices and the associated interface states in one-dimensional plasmonic crystals. *Phys. Rev. B* **2022**, *106* (4), 045401−045409.
(55) Bleckmann, F.; Cherpakova, Z.; Linden, S.; Alberti, A. Spectral imaging of topological edge states in plasmonic waveguide arrays. *Phys. Rev. B* **2017**, *96* (4), 045417−045422.
(56) Rappoport, T. G.; Bludov, Y. V.; Koppens, F. H. L.; Peres, N. M. R. Topological graphene plasmons in a plasmonic realization of the Su-Schrieffer-Heeger model. *ACS Photonics* **2021**, *8* (6), 1817−1823.
(57) Kruk, S.; Slobozhanyuk, A.; Denkova, D.; Poddubny, A.; Kravchenko, I.; Miroshnichenko, A.; Neshev, D.; Kivshar, Y. Edge states and topological phase transitions in chains of dielectric nanoparticles. *Small* **2017**, *13* (11), 1603190−1603195.
(58) Xiao, Y.-X.; Ma, G.; Zhang, Z.-Q.; Chan, C. T. Topological subspace-induced bound state in the continuum. *Phys. Rev. Lett.* **2017**, *118* (16), 166803−166807.
(59) Obana, D.; Liu, F.; Wakabayashi, K. Topological edge states in the Su-Schrieffer-Heeger model. *Phys. Rev. B* **2019**, *100* (7), 075437−075445.
(60) Yuce, C.; Ramezani, H. Topological states in a non-Hermitian two-dimensional Su-Schrieffer-Heeger model. *Phys. Rev. A* **2019**, *100* (3), 032102−032106.
(61) Harder, T. H.; Sun, M.; Egorov, O. A.; Vakulchyk, I.; Beierlein, J.; Gagel, P.; Emmerling, M.; Schneider, C.; Peschel, U.; Savenko, I. G.; Klembt, S.; Höfling, S. Coherent topological polariton laser. *ACS Photonics* **2021**, *8* (5), 1377−1384.
(62) Gao, T.; Estrecho, E.; Bliokh, K. Y.; Liew, T. C. H.; Fraser, M. D.; Brodbeck, S.; Kamp, M.; Schneider, C.; Höfling, S.; Yamamoto, Y.; Nori, F.; Kivshar, Y. S.; Truscott, A. G.; Dall, R. G.; Ostrovskaya, E. A. Observation of non-Hermitian degeneracies in a chaotic exciton-polariton billiard. *Nature* **2015**, *526* (7574), 554−558.
(63) Klembt, S.; Harder, T. H.; Egorov, O. A.; Winkler, K.; Ge, R.; Bandres, M. A.; Emmerling, M.; Worschech, L.; Liew, T. C. H.; Segev, M.; Schneider, C.; Höfling, S. Exciton-polariton topological insulator. *Nature* **2018**, *562* (7728), 552−556.
(64) Feng, F.; Si, G.; Min, C.; Yuan, X.; Somekh, M. On-chip plasmonic spin-Hall nanograting for simultaneously detecting phase and polarization singularities. *Light: Science & Applications* **2020**, *9* (1), 95−103.
(65) Yang, Z.; Huang, P.-S.; Lin, Y.-T.; Qin, H.; Zúñiga-Pérez, J.; Shi, Y.; Wang, Z.; Cheng, X.; Tang, M.-C.; Han, S.; Kanté, B.; Li, B.; Wu, P. C.; Genevet, P.; Song, Q. Creating pairs of exceptional points for arbitrary polarization control: asymmetric vectorial wavefront modulation. *Nat. Commun.* **2024**, *15* (1), 232−240.
(66) Zhao, X.; Li, Z.; Geng, G.; Liu, W.; Cheng, J.; Cheng, H.; Chen, S. Mode-interference-induced chiral exceptional points in momentum space. *Laser & Photonics Reviews* **2024**, *18* (7), 2301257−2301265.
(67) Deng, Z. L.; Li, F. J.; Li, H.; Li, X.; Alù, A. Extreme diffraction control in metagratings leveraging bound states in the continuum and exceptional points. *Laser & Photonics Reviews* **2022**, *16* (6), 2100617−2100622.
(68) Zak, J. Berry's phase for energy bands in solids. *Phys. Rev. Lett.* **1989**, *62* (23), 2747−2750.
(69) Bai, Q.; Perrin, M.; Sauvan, C.; Hugonin, J. P.; Lalanne, P. Efficient and intuitive method for the analysis of light scattering by a resonant nanostructure. *Opt. Express* **2013**, *21* (22), 27371−27382.

https://doi.org/10.1021/acs.nanolett.5c00144
Nano Lett. 2025, 25, 6117−6124